



Triple-phase oxygen electrocatalysis of hollow spherical structures for rechargeable Zn-Air batteries

Chen-Chen Weng^a, Jin-Tao Ren^a, Hao-Yu Wang^a, Xian-Wei Lv^a, Yue-Jun Song^b, Yan-Su Wang^a, Lei Chen^a, Wen-Wen Tian^a, Zhong-Yong Yuan^{a,*}

^a Key Laboratory of Advanced Energy Materials Chemistry (Ministry of Education), School of Materials Science and Engineering, Nankai University, Tianjin 300350, China

^b China People's Police University, Langfang 065000, Hebei Province, China

ARTICLE INFO

Keywords:

Solid-liquid-gas interface
Sulfur incorporation
Bifunctional ORR/OER electrocatalysts
Electrocatalysis
Zn-air batteries

ABSTRACT

The high-efficient and low-cost oxygen electrocatalysts are of significant importance but challenge in energy storage and conversion devices. The oxygen electrocatalysis involves triple-phase interfaces of solid catalyst, liquid electrolyte and gaseous oxygen. The reaction microenvironment in which the ample transmission pathway sufficiently feeds the highly active sites and expulses product rapidly is typically desired. Herein, the reaction interface microenvironment of hollow spherical bimetallic electrocatalyst (CoFe-SNC) is regulated via structural architecture engineering, achieving the ample triple-phase contact points of O₂ (gas), electrolyte (liquid) and electrocatalyst (solid). Sufficient O₂ supply and unimpeded mass transfer afforded by triple-phase interface flourish catalytic efficiency and enhance oxygen electrocatalysis. Simultaneously the incorporation of sulfur dopant improves the intrinsic catalytic activity, giving rise to highly active sites in reaction interface of CoFe-SNC. With such well-constructed triple-phase interface microenvironment, the CoFe-SNC shows outstanding oxygen reduction reaction activity ($E_{1/2} = 0.86$ V vs RHE) and stability in basic media, and a low charging-discharging voltage gap (1.19 V) with excellent durability is realized in rechargeable Zn-air batteries.

1. Introduction

The aggravated energy crisis and accompanying environmental contamination caused by excessive dependence on the fossil fuels have been stimulating substantial efforts on the exploration of environment-friendly and effective energy conversion and storage devices such as fuel cells and metal-air batteries [1–5]. To optimize efficiency of such sustainable energy technologies, the development of highly-efficient bifunctional electrocatalysts towards oxygen electrocatalysis including oxygen reduction reaction (ORR) and oxygen evolution reaction (OER) is highly desired to promote sluggish reaction kinetics [6–9]. It is generally recognized that noble metal-based electrocatalysts including Pt, IrO₂ display the superior catalytic activity. However, the prohibitive cost and less-than-ideal durability hinder their widespread commercial applications [10]. Hence, cost-efficient alternatives with remarkable electrocatalytic activity and excellent stability for oxygen electrocatalysis are of inevitability for developing advanced rechargeable metal-air batteries [11–13].

The ORR process, a gas consuming reaction, occurs on the solid-liquid-gas triple-phase interfaces in which electron and ion/molecule contact at electrocatalytic active sites [14,15]. In actual reaction condition, the microenvironment of electrocatalyst underwater significantly affects the reaction interface. Regulating the infiltration of electrocatalyst surface by electrolyte can impose a prominent impact on forming triple-phase interface of air, electrolyte and electrocatalyst, in which the rapid entry and exit of gas and electrolyte can be realized, consequently leading to an accelerated reaction rate [16,17]. Thus, neither fully flooded by electrolyte nor covered by continuous air cushions, the electrocatalyst surface is expected to trap proper air pockets among the electrolyte soak to give rise to the formation of ample triple-phase interface in their structural architecture. Therefore, both the fluent ion transmission and sufficient O₂ supply can be guaranteed [18]. On the other hand, as for OER process, a gas evolution reaction, the product oxygen is produced on the surface of electrocatalyst. It has been reported that the well-designed micro-/nanoscale structure in electrocatalyst surface is conducive to repel the as-formed gas bubble and

* Corresponding author.

E-mail address: zyyuan@nankai.edu.cn (Z.-Y. Yuan).

<https://doi.org/10.1016/j.apcatb.2022.121190>

Received 11 December 2021; Received in revised form 29 January 2022; Accepted 4 February 2022

Available online 8 February 2022

0926-3373/© 2022 Elsevier B.V. All rights reserved.

mitigate the pinning effect of bubbles on the surface [19,20]. However, apart from expediting gas bubbles departure, another severe problem still exists. Based on the Kelvin equation, inside a liquid environment, the newly-produced tiny bubbles with the ultra-small radius afford extremely low vapor pressure, which constitutes the bottleneck for the formation of bubbles. The excess energy is required to drive the as-produced O_2 molecules to form bubbles, giving rise to an increased overpotential. Thus, the introduction of gas seed can avoid this energy-consuming bubble formation process. In this context, the triple-phase contact region can provide large amount of available gas seed under reaction condition, which enables a highly energy-efficient gas evolution scenario. Therefore, the triple-phase interface engineering exerts significant effect in promoting catalytic efficiency of bifunctional ORR/OER electrocatalysts.

During the past several years, nitrogen-coordinated transition metals anchored on carbon (TM-N-C) catalysts have been demonstrated to be the most promising electrocatalytic materials due to the abundant reserves and considerable catalytic performance [21–25]. In view of reversible oxygen electrocatalysis driven by one catalyst, joint construction of the energetic ORR-active and OER-active structure by bimetal doping, such as Fe and Co, Fe and Ni, has been proposed to be the rational strategy for excellent bifunctional ORR/OER electrocatalysis [7,26–29]. The recent progress has witnessed the development of bimetal TM-N-C catalysts. In order to provide the applicable alternatives to precious-metal-based materials, the active sites of TM-N-C catalysts should deliver the high intrinsic ability to break and form the covalent bonds $O=O$ and $O-H$. Alternatively, the heteroatom sulfur (S) has been found efficient to promote electrocatalytic activity by modifying TM-N-C active centers [30,31]. Similar to nitrogen, S is a *p*-block element, but it should be noted that the S atoms possess different electron spin density and relatively low electronegativity. When incorporated into carbon skeleton, the S atoms commonly produce the thiophene-like structures (C-S-C). Although the C-S-C sites show the unsatisfactory activity for oxygen electrocatalysis, the C-S-C sites can exert a long-range interaction with the metal active centers, which can make an effect on reducing the electron localization of TM-N-C, thus improving intrinsic electrochemical reactivity [17,32–34].

Hence, designing an electrocatalyst which combines the ample triple-phase interface and modified active sites should be an effective way to boost oxygen electrocatalysis. So far, many researchers are committed to constructing gas diffusion electrode (GDE), which commonly consists of hydrophobic agents such as poly(tetrafluoroethylene) (PTFE). The GDE affords the fast oxygen transmission without the need of gas dissolution in the electrolyte. However, the introduction of insulating PTFE inevitably retards electron transport and covers active sites, thus resulting in the activity decay. To progress toward improving reaction microenvironment and simultaneously retain intrinsic catalytic ability, regulating the structural architecture of electrocatalyst to render a moderate electrolyte infiltration is proposed as a rational method.

Herein, Fe and Co atoms anchored in the N,S-codoped hollow carbon spheres (CoFe-SNC) with well-constructed structural architecture were prepared to enable the ample gas-liquid-solid triple-phase interface and S-modulated active sites. The introduction of S dopant in CoFe-SNC allows for a synergistic effect between S-dopant and TM-N-C active sites, which conduces to improve intrinsic activity and accelerate reaction kinetics. Furthermore, the Zn-air battery test unravels that regulating the catalyst structure to establish maximum triple-phase interface can make a contribution on boosting Zn-air battery performance. It is demonstrated that the smooth and continuous mass transfer imparted by the ample gas-liquid-solid triple-phase interface of CoFe-SNC is able to facilitate the oxygen electrocatalysis in actual Zn-air operation. Profited from the ample triple-phase contact region and the reinforced intrinsic activity, the impressive electrochemical activity and Zn-air battery performance are realized including excellent activity and robust stability.

2. Experimental section

2.1. Materials

All chemicals and reagents were used without further purification. Styrene (C_8H_8 , CP), azodiisobutyronitrile (AIBN) and carbon block (VXC-72R) were obtained from Meryer Chemistry Co., Ltd. Sodium dodecyl sulfate (SDS, $C_{12}H_{25}NaO_4S$, AR) and 3-Hydroxytyramine hydrochloride (dopamine, AR) were bought from ShangHai D&B Biological Science and Technology Co., Ltd. Cobalt acetate tetrahydrate ($Co(Ac)_2 \cdot 4 H_2O$, AR), potassium peroxydisulfate ($K_2S_2O_8$, AR, 99.5%), concentrated sulfuric acid solution (98%) and ferric chloride tetrahydrate ($FeCl_3 \cdot 4 H_2O$, AR) were bought from TianJin Chemistry Co., Ltd. Polyvinylpyrrolidone (PVP, AR) was obtained from Macklin Biological Science and Technology Co., Ltd. Ammonia aqueous solution (NH_4OH , GR, 30 wt%) and hydrogen peroxide H_2O_2 , GR 30% were bought from TianJin DaMao Chemical Reagent Co., Ltd. Nafon (5 wt%) was bought from Sigma-Aldrich. AR and GR are the abbreviations of analytical reagent and guaranteed reagent, respectively.

2.2. Preparation of catalysts

Synthesis of polystyrene sphere (PS) with radius of 50 nm (PS-50): The PS-50 was prepared by an emulsion polymerization method. Briefly, 0.1 g SDS and 10 mL of styrene were added into 56 mL distilled water. The obtained mixture was deaerated by nitrogen purging for 1 h. Then, 0.03 g $K_2S_2O_8$ was added under vigorously stirring followed by heating to 80 °C. The mixture was kept at 80 °C for 6 h under magnetic stirring with N_2 purging. The clear solution turned into a milk white and opaque solution. The PS-50 was gathered via centrifugation at 8000 rpm after being washed by ethanol. Finally, the as-prepared PS-50 was placed in an oven at 80 °C overnight.

Synthesis of PS with radius of 200 nm (PS-200): 0.11 g SDS and 0.1 g $K_2S_2O_8$ were added in a mixed solution of 50 mL ethanol and 20 mL distilled water. 4.5 mL styrene was added under vigorous stirring with nitrogen purging. The reaction was heated to 70 °C for 8 h. The PS-200 was gathered via centrifugation at 8000 rpm after being washed by ethanol. Finally, PS-200 was placed in an oven at 80 °C overnight.

Synthesis of PS with radius of 500 nm (PS-500): The PS-500 was prepared by a dispersion polymerization method. 11.7 g styrene and 0.97 g AIBN were dispersed in a solution containing 20 g distilled water and 60 g ethanol. The mixture was deaerated by nitrogen purging under vigorous stirring. Then, 4.88 g PVP was dispersed in the above solution. Keep the mixture at 70 °C for 6 h with continuously purging nitrogen. The PS-500 was gathered via centrifugation at 8000 rpm after being washed. Finally, PS-500 was placed in an oven at 80 °C overnight.

Synthesis of PS with radius of 4000 nm (PS-4000): The PS-4000 was prepared by a dispersion polymerization method. 6.43 g styrene and 0.92 g AIBN were dispersed in a solution containing 20 g distilled water and 60 g ethanol. The mixture was deaerated by nitrogen purging under vigorous stirring. Then, 4.6 g PVP was dispersed into the above solution. Keep the mixture at 70 °C for 6 h with continuously purging nitrogen. The PS-4000 was gathered via centrifugation at 8000 rpm after being washed by ethanol. Finally, PS-4000 was placed in an oven at 80 °C overnight.

Synthesis of sulfonated polystyrene sphere with radius of 200 nm (S-PS-200), sulfonated carbon block (VXC-72R) and H_2O_2 -treated PS: 2 g PS-200 was leached in concentrated sulfuric acid solution. Followed by 30 min continuous ultrasonic treatment, the above suspension was vigorously stirred for 6 h. Then, the S-PS-200 was gathered via centrifugation at 8000 rpm after being washed. S-PS-200 was dried in an oven at 80 °C overnight. The synthesis of H_2SO_4 -treated VXC-72R(S-VXC) was similar to that of S-PS-200 except that the VXC-72R was used to replace PS-200. The H_2O_2 -treated PS was prepared in the same procedure as S-PS-200 except that the concentrated sulfuric acid solution was replaced by H_2O_2 solution.

Synthesis of CoFe-NC-x: The PS-50, PS-200, PS-500 and PS-4000 were used to prepare CoFe-NC-x with the radius of 50, 200, 500 and 4000 nm. In a typical reaction, 0.1 g PS template was mixed with 30 mL distilled water. After ultrasonic treatment for 1 h, 0.5 g dopamine was dissolved in above suspension. Then, 5 mL of aqueous solution which contained 0.0067 g $\text{Co}(\text{Ac})_2 \cdot 4 \text{H}_2\text{O}$ and 0.0031 g $\text{FeCl}_3 \cdot 4 \text{H}_2\text{O}$ was injected. Under vigorously stirring, the NH_4OH (30 wt%) was dropwise added into the obtained solution to give a pH of around 8.5. After polymerization for 10 h, the CoFePDA@PS precursors were formed and collected by vacuum filtration. The CoFePDA@PS precursors were dried in oven at 80 °C. The CoFePDA@PS precursors were pyrolyzed at 800 °C for 2 h under flowing N_2 atmosphere.

Synthesis of SNC, CoFe-SNC, CoFe-S-VXC and CoFe-ONC: The synthesis procedure of CoFe-SNC, CoFe-S-VXC and CoFe-ONC were same as the CoFe-NC-x except that the S-PS, S-VXC and H_2O_2 -treated PS were employed as the templates, respectively. The fabrication of SNC was same as CoFe-SNC except that both $\text{FeCl}_3 \cdot 4 \text{H}_2\text{O}$ and $\text{Co}(\text{Ac})_2 \cdot 4 \text{H}_2\text{O}$ were absent during synthesis process.

Synthesis of CoFe-SNC-1, CoFe-SNC-3 and CoFe-SNC-4: The synthesis procedure of CoFe-SNC-1, CoFe-SNC-3 and CoFe-SNC-4 were same as the CoFe-SNC except the amount of metal. To prepare CoFe-SNC-1, 0.013 mmol $\text{Co}(\text{Ac})_2 \cdot 4 \text{H}_2\text{O}$ and 0.006 mmol $\text{FeCl}_3 \cdot 4 \text{H}_2\text{O}$ was used. As for CoFe-SNC-3, $\text{Co}(\text{Ac})_2 \cdot 4 \text{H}_2\text{O}$ was 0.25 mmol and $\text{FeCl}_3 \cdot 4 \text{H}_2\text{O}$ was 0.12 mmol. In the synthesis procedure of CoFe-SNC-4, 5 mmol $\text{Co}(\text{Ac})_2 \cdot 4 \text{H}_2\text{O}$ and 2 mmol $\text{FeCl}_3 \cdot 4 \text{H}_2\text{O}$ were used.

Synthesis of crushed CoFe-SNC: The CoFe-SNC was crushed by grinding under liquid nitrogen to produce the crushed CoFe-SNC.

The physicochemical characterizations and electrochemical measurements are provided in the [Supporting Information](#).

3. Results and discussion

3.1. The improved triple-phase interface of catalyst

As is well known, when the surface of solid is immersed into a liquid

system there are three typical interfaces ([Fig. S1, Supporting Information](#)): (1) Wenzel state (UW-state) features the complete soak on the solid surface by liquid without gas at interface; (2) Wenzel-Cassie coexistent state (UWC-state), in which the solid surface is partially wetted by liquid with certain amount of air trapped among the liquid, enables the gas-liquid-solid triple-phase interface; (3) Cassie state (UC-state) accommodates the quasi-continuous gas layer between solid surface and liquid, presenting few solid-liquid contact. Herein, to render electrocatalysts with decent reaction interface, hollow carbon spheres decorated with Fe and Co species were fabricated and their internal diameters were adjusted from 50 to 4000 nm (CoFe-NC-x, x represents the internal diameter). As schematically illustrated in [Fig. S2](#), the CoFe-NC-x with well-defined hollow spherical structures were fabricated via a polymeration-pyrolysis process. Firstly, the uniform polystyrene spheres (PSs) were pre-synthesized and employed as hard templates ([Fig. S3](#)). The PSs were dispersed in deionized water by sonication, followed by the addition of dopamine. Upon vigorously stirring, an aqueous solution containing cobalt acetate tetrahydrate ($\text{Co}(\text{Ac})_2 \cdot 4 \text{H}_2\text{O}$) and ferric chloride tetrahydrate ($\text{FeCl}_3 \cdot 4 \text{H}_2\text{O}$) were injected into the obtained solution. The NH_4OH (30 wt%) was used to provide a weakly alkaline environment. The polydopamine (PDA) was produced on the surface of PSs, and the abundant catechol groups of PDA can effectively chelate Fe^{3+} and Co^{2+} , yielding the precursor CoFePDA@PS. The CoFePDA@PS was pyrolyzed under N_2 atmosphere at 800 °C, yielding the CoFe-NC-x. The pyrolysis process not only led to the removal of PS templates but also converted CoFePDA@PS to the highly active TM-N-C catalyst. In [Fig. 1a](#), the CoFe-NC-50 exhibits the hollow sphere morphology with good uniformity, which results from the reverse replication of PS templates. When the PS templates with enlarged sizes (from 200 to 4000 nm) were used, the CoFe-NC-200, CoFe-NC-500 and CoFe-NC-4000 can be obtained and all of them retain the hollow spherical structure ([Fig. 1a-d](#)).

The solid-liquid-gas triple-phase interface is determined by liquid spread state on the solid surface underwater. All the as-prepared electrocatalysts are demonstrated to be highly hydrophilic with the contact-

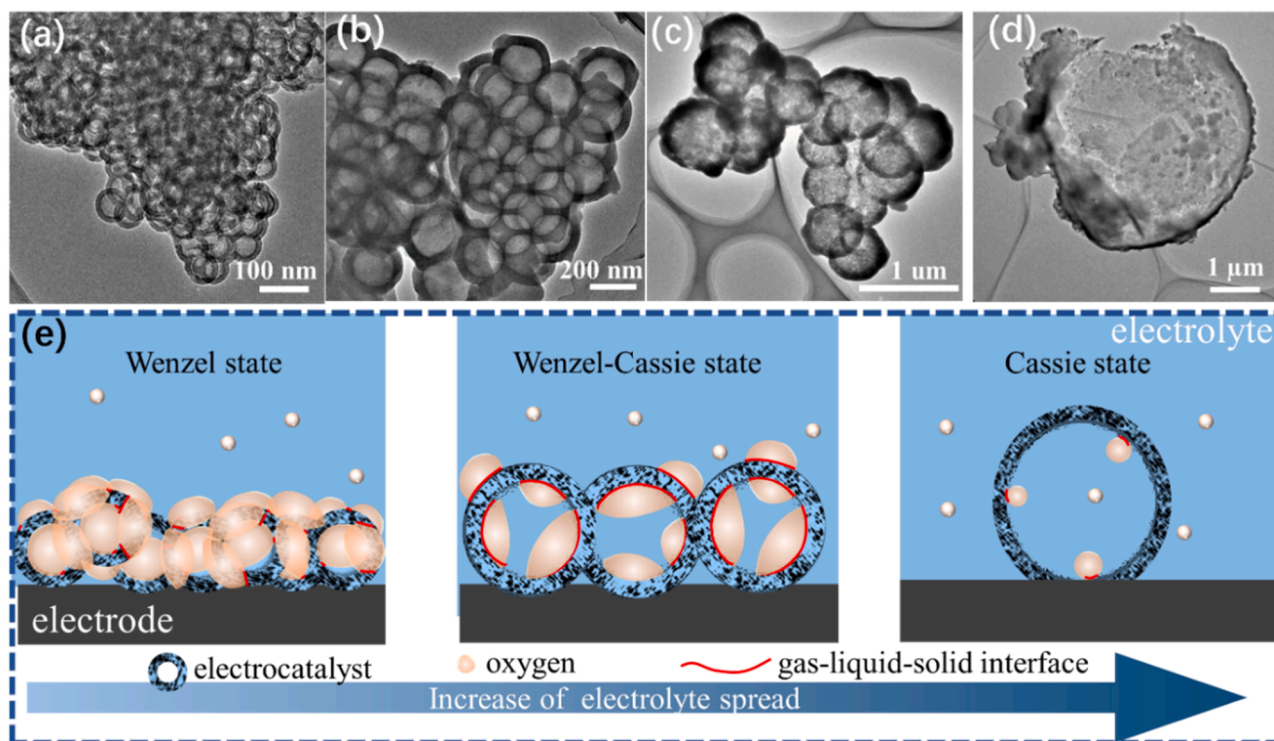


Fig. 1. TEM images of (a) CoFe-NC-50, (b) CoFe-NC-200, (c) CoFe-NC-500, (d) CoFe-NC-4000, (e) Schematic cartoon of electrolyte spread state on the hollow CoFe-NC-x.

angles of nearly 0° (Fig. S4). However, it has been well-established that in spite of a very small water contact angle, the formation of a liquid coating layer on a fresh dry surface is difficult when the solid surface is highly curved [35–37]. Based on the calculation (see more details in Appendix, Supplemental Information), the surface with low curvature is prone to being flooded by liquid, whereas the highly curved surface delivers a high repellency to the liquid spread. The diverse surface curvatures of hollow CoFe-NC-*x* can lead to the distinct spread state of electrolyte on catalyst surface. As for the sample of CoFe-NC-50, the high surface curvature in mesoporous hollow spheres enable a reinforced air trap and consolidated air cushion underwater. In contrast, the decreased curvature afforded by the increased internal diameter gives rise to incremental electrolyte infiltration (Fig. 1e).

As a promising energy-conversion device, Zn-air batteries feature environmental benignity and high theoretical energy densities. The actual performance of Zn-air battery is remarkably affected by the cathodic electrode, in which the ORR accounts for discharging process, while the OER plays an important role in the charging process. The discharge-charge performance of the as-prepared CoFe-NC-*x* was assessed on a homemade Zn-air battery. In Fig. 2, the CoFe-NC-200 reveals a discharge-charge voltage gap of 1.10 V at 30 mA cm^{-2} , which is lower than those of CoFe-NC-50 (1.23 V), CoFe-NC-500 (1.50 V), and CoFe-NC-4000 (1.34 V). In the discharging process, in comparison with the tardive increase in current density of other CoFe-NC-*x* samples, the CoFe-NC-200 demonstrates a flat slope in discharge polarization curve accompanied by a high current-density ceiling of 143.9 mA cm^{-2} at 0.4 V. A similar straightened trend in polarization curve is also found in the charging process of CoFe-NC-200, eventually affording a charging current density ceiling of 115.2 mA cm^{-2} . To be noted, the different charging-discharging behaviors are not possible to stem from the distinction of BET surface area as CoFe-NC-500 possesses the highest BET surface area ($654 \text{ cm}^2/\text{g}$) among the series (Fig. S5, CoFe-NC-4000: $439 \text{ cm}^2/\text{g}$, CoFe-NC-200: $455 \text{ cm}^2/\text{g}$, CoFe-NC-50: $573 \text{ cm}^2/\text{g}$).

As both the ORR and OER occur in the triple-phase interface of solid electrocatalyst, liquid electrolyte and gaseous reactants/products, the triple-phase interface on the cathodic catalysts is of significant importance for implementing the intrinsic catalytic ability. The CoFe-NC-50 with high curvature possesses the strong capacity of gas accommodation and the limited access for electrolyte infiltration. This feeble electrolyte permeation on the textured surface gives numerous gas-solid interface (UC-state) on CoFe-NC50, which is bad for cathodic discharging process. This disadvantage can be gradually overcome as the gas-consuming ORR proceeds as reflected by the discharging behavior of CoFe-NC-50. More specifically, the discharging performance of CoFe-NC-50 gradually meliorates with respect to two stages with distinguishing current increase speeds in polarization curve: 14.2 mA cm^{-2} per 100 mV from 1.25 V to 0.97 V and 19.37 mA cm^{-2} per 100 mV from 0.96 V to 0.4 V. This phenomenon may be caused by the fact that as

reaction proceeds, the gas cushion between electrode and electrolyte is continuously consumed and reinforced immersion of CoFe-NC-50 in electrolyte leads to the increased gas-liquid-solid triple-phase contact, thus accelerating the discharge reaction in second stage of 0.96–0.4 V. Furthermore, the contour of discharging polarization curves on CoFe-NC-200 and CoFe-NC-4000 is investigated. At the beginning of discharging reaction, CoFe-NC-200 and CoFe-NC-4000 share the approximate current increase speed within the range from 0 to 12 mA cm^{-2} . Subsequently, the discharging current density increases as fast as 17.91 mA cm^{-2} per 100 mV from 1.0 V to 0.8 V on CoFe-NC-200, while only 11.81 mA cm^{-2} per 100 mV current increase is observed on CoFe-NC-4000. The CoFe-NC-200 with a favorable structural architecture possesses the moderate surface curvature, which features the Wenzel-Cassie coexistent state (UWC-state). The maximum coexistence of gas-solid contact and liquid-solid contact gives rise to the decent triple-phase interface, which imposes a prominent impact on accelerating transmission of both gas and electrolyte, consequently promoting the reaction rate of discharging process. Further decrease in surface curvature on CoFe-NC-500 and CoFe-NC-4000 leads to increased liquid-solid interface. The low and negligible curvature indulge the electrolyte to flood the surface. Thus, the feebly catalytic behavior of CoFe-NC-4000 is reasonable for the poor gaseous feed in solid-liquid interface. Therefore, as for highly-curved CoFe-NC-50 and lowly-curved catalysts including CoFe-NC-500 and CoFe-NC-4000, the lack of either liquid-solid or gas-solid interface significantly retards the reaction rate due to the deficiency of ion or oxygen during discharging process. In contrast, the CoFe-NC-200 is able to accommodate appropriate gas phase to produce maximum triple-phase interface, warranting efficient mass transfer and sufficient reactant supply.

In the charging process, the formation of bubbles inside a liquid environment is an energy-consuming process, which needs to overcome the extremely low vapor pressure of initial bubble with tiny volume. The introduction of gas seeds is of key importance in promoting gas bubble production. Analog to the addition of zeolite into a heated liquid, the favorable triple-phase interface in CoFe-NC-200 holds large number of accessible gas seeds, which benefits for the as-produced O_2 molecules to form bubbles. This process eliminates the energy-consuming bubbles generation process and renders a highly-efficient gas formation in charging process.

To validate the significant importance of moderate hollow structure on the discharge-charge performance, CoFe-NC-200 was ground in liquid nitrogen to crush the hollow sphere and the obtained sample was named as C-CoFe-NC-200. It can be seen that the hollow structure is cracked in C-CoFe-NC-200 (Fig. S6). The discharge polarization curve of C-CoFe-NC-200 arcs with the increased current density. A sluggish charging behavior is also observed in the charge process of C-CoFe-NC-200. Compared with CoFe-NC-200, the feeble discharge-charge performance of C-CoFe-NC-200 confirms that the decent triple-phase interface afforded by the hollow architecture holds the key for improving the Zn-air battery performance. The small fragment of hollow sphere on C-CoFe-NC-200 suffers from the incomplete winding surface, which is failed to accommodate gas cushion. The minimal triple-phase interface results in feeble discharge-charge performance upon the hollow structure of CoFe-NC-200 is cracked. This confirms the favorable triple-phase interface afforded by the hollow architecture with moderate surface curvature holds the key for improvement of liquid Zn-air battery performance. Thus, the rational adjustment over the surface curvature of electrocatalysts for the favorable gas-liquid-solid interface provides a significant opportunity to promote mass transfer and boost reaction efficiency in Zn-air battery operation.

3.2. The boosted intrinsic activity via S-doping

The PS template with diameter of 200 nm (PS-200) was subjected to a sulfuric acid leaching, and the sulfonated PS-200 (S-PS-200) inherited compactly arranged spherical structure with unchanged diameter of ca.

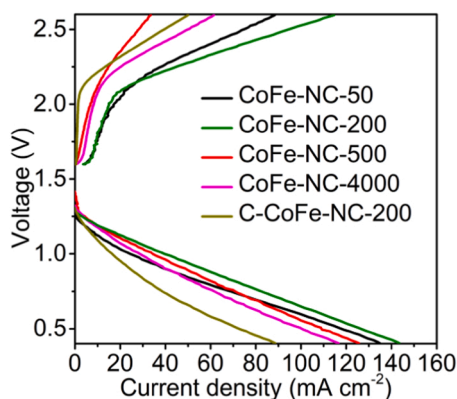


Fig. 2. The charge-discharge polarization curves of the liquid Zn-air batteries assembled with the as-prepared catalysts.

200 nm (Fig. S7a). The synthesis of S-doped CoFe-NC-200 (named as CoFe-SNC) was similar to CoFe-NC-200 except that PS-200 was replaced by S-PS-200. The bifunctional template, S-PS-200, not only accounted for S doping but also led to the formation of hollow spherical structure. CoFe-NC-200 is used as control sample and hereinafter referred to as CoFe-NC. According to the IR spectra (Fig. S8), for both PS-200 and S-PS-200, the peaks located at 698, 754, 1449, and 1493 cm^{-1} are assigned to polystyrene component [38]. After sulfuric acid leaching, the absorption bands at 1190–1200 cm^{-1} and 1020–1130 cm^{-1} appear, which present the asymmetric and symmetric stretching modes of $\text{O}=\text{S}=\text{O}$, respectively. The emergence of absorption band at 573–629 cm^{-1} results from the stretching mode of $\text{S}-\text{O}$ [39]. Thus, the PS-200 is confirmed to be functionalized with $-\text{SO}_3\text{H}$ by sulfuric acid leaching. After polydopamine coating, the peak centered at 1431 cm^{-1} corresponds to heterocyclic stretching ($\text{C}-\text{N}$ bonds) and the peak at 1040 cm^{-1} arises from $\text{C}-\text{H}$ in-plane deformation [40,41]. After pyrolysis, the S-PS-200 as bifunctional-template enables the resultant CoFe-SNC with hollow spherical structure and incorporation of S dopant.

The three-dimensional (3D) interconnected hollow spherical structure of CoFe-SNC were examined by SEM measurement (Fig. 3a). The unique structure of CoFe-SNC is the result of the faithful replica of periodic colloidal S-PS-200 templates. It can be clearly seen that macropores with a diameter of approximately 200 nm are assembled in a hexagonal array and the neighboring macropores are interconnected by mesopores. Well-interconnected 3D hollow nanosphere architecture is observed in TEM treatment (Fig. 3b). In Fig. 3c, the faithful replica of PS templates and subsequent thermal removal give rise to rich cavity with curved surface, which is expected to enlarge and consolidate triple-phase interface [42–44]. Notably, no obvious metal-containing nanoparticles can be observed, implying that Co and Fe species are uniformly confined in the N, S-codoped carbon skeleton. Fig. 3d indicates that the N, S, O, Co, Fe and C elements are evenly distributed, and it is revealed that the S is incorporated into the hollow carbon spherical structure. In the XRD pattern of CoFe-SNC (Fig. S9), two broad peaks centered at 25° and 44° (2 θ) correspond to carbon (002) and (101) diffractions respectively, suggesting that the precursor has been carbonized after pyrolysis. No other obvious diffraction peaks can be seen, suggesting the absence of crystalline phases including metallic CoFe or CoFe compounds (sulfide, oxide, carbide, and/or nitride).

XPS was used to demonstrate the chemical state of the elements in the obtained catalysts. The N contents of CoFe-SNC and CoFe-NC are 3.8 and 3.4 atom%, respectively (Fig. 4a). The bonding status of N in CoFe-

SNC and CoFe-NC were analyzed, and four characteristic N species are observed including pyridinic-N (398.4 eV), pyrrolic-N (400.1 eV), graphitic-N (401.1 eV), and oxidized N (403.1 eV). The O contents are measured to be 6.6% for CoFe-SNC and 5.2% for CoFe-NC. In the high resolution XPS O 1s spectra, both CoFe-SNC and CoFe-NC show ketonic $\text{C}=\text{O}$ (531.2 ± 0.3 eV) groups and epoxide $\text{C}-\text{O}-\text{C}$ or hydroxyl $\text{C}-\text{OH}$ (533.1 ± 0.3 eV) groups (Fig. S10a). Note that there is no obvious O species associated with the metal oxide centered at 529–530 eV, indicating the absence of metal oxide. XPS discloses that the Co contents of CoFe-SNC and CoFe-NC are 0.38% and 0.54%, and the Fe contents are detected to be 0.31% and 0.4%, respectively. As for Co 2p spectra, after deconvolution, the valence state of Co species is situated between that of Co^{III} and Co^{II} [45]. Neither metallic states Co species (centered at 778.2 eV) nor metallic states Fe species (centered at 706.7) is detected in Co and Fe XPS spectra, indicating that the Co and Fe are not metallic state (Fig. S10b, c) [46,47]. For both CoFe-NC and CoFe-SNC, the N1s spectra display emergence of peaks at 399.5 eV [27], which are caused by the fact that the pyridinic N and pyrrolic N have been established to anchor TM atoms with the assistance of lone pair electrons, forming transition metal-coordinated nitrogen (TM-N) [48–50]. Besides, the S doping in the CoFe-SNC is also reflected by XPS analysis with a S content of 0.44%. In the deconvoluted high-resolution S 2p spectra (Fig. 4b), the peaks at 164 and 165.2 eV are assigned to the $\text{S}2\text{p}_{3/2}$ and $\text{S}2\text{p}_{1/2}$ states of thiophene-like structure, and the peak at 168.5 eV results from oxidized sulfur groups [30,32]. Notably, similar to CoFe-NC, CoFe-SNC is free from metal–sulfur interaction in TM (Fe and Co) 2p spectra (Fig. S10b, c) and no metal–sulfur bonds can be found in S 2p spectra. Accordingly, the S is only incorporated into the aromatic carbon skeleton to afford C-S-C motif. It has been reported that the C-S-C sites can contribute to reducing electron localization around TM centers via long-range interaction, thus giving rise to the synergistic effects between C-S-C and TM centers to decrease ORR activation barrier on TM-N-C [11,12].

The electrocatalytic activity of as-obtained samples were evaluated through the RDE measurement in O_2 -saturated 0.1 M KOH solution. Firstly, the influence of metal dosages is investigated. The control samples CoFe-SNC-4, CoFe-SNC-3 and CoFe-SNC-1 were synthesized based on varied metals amount and the metal dosages increased in the order of CoFe-SNC-1, CoFe-SNC, CoFe-SNC-3 and CoFe-SNC-4. Among the series, CoFe-SNC delivers an excellent ORR activity with a half-wave potentials ($E_{1/2}$) of 0.86 V. Upon decreasing the amount of metal dosage, the CoFe-SNC-1 shows the dissatisfactory ORR activity with respect to $E_{1/2}$ (0.85 V), 10 mV lower than that of CoFe-SNC (Fig. S11a). As for the increased metal dosages, both CoFe-SNC-3 and CoFe-SNC-4 reveal the

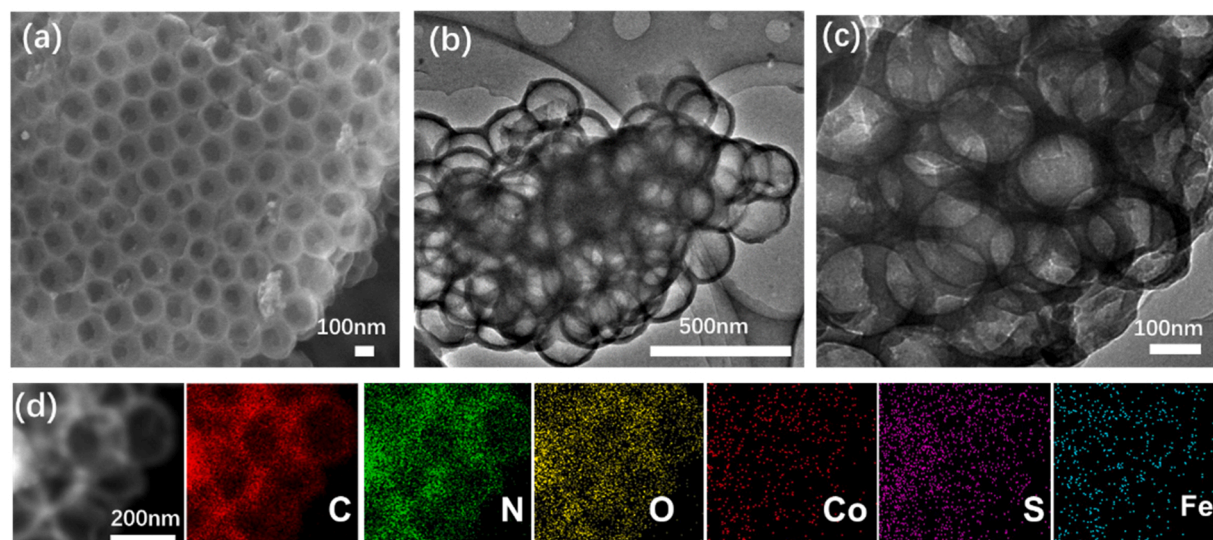


Fig. 3. (a) SEM image of CoFe-SNC, (b) TEM image of CoFe-SNC, (c) TEM image of CoFe-SNC, (d) EDS element mapping of CoFe-SNC.

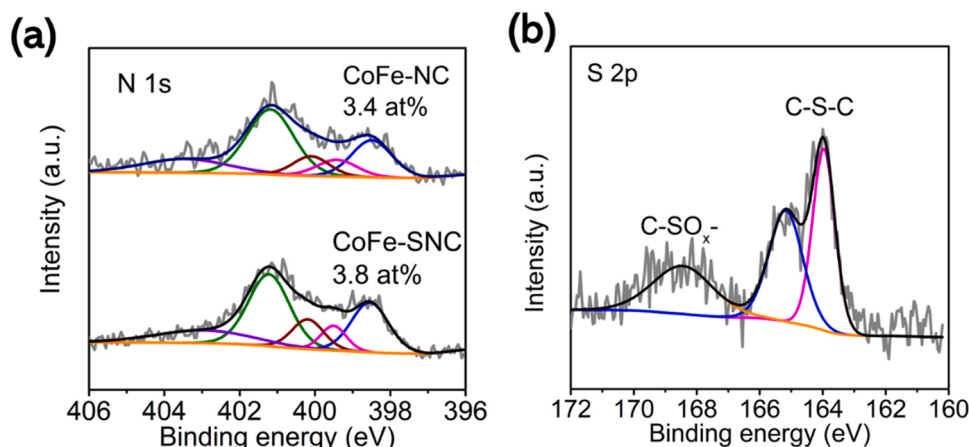


Fig. 4. (a) N 1 s XPS spectra of CoFe-NC and CoFe-SNC, (b) S 1 s XPS spectra of CoFe-SNC.

sluggish ORR catalysis process. The $E_{1/2}$ of CoFe-SNC-3 and CoFe-SNC-4 are 0.82 V and 0.78 V, respectively, both of which are lower than that of CoFe-SNC. Further structural characterization sheds light on the structure of control samples. In the TEM image of CoFe-SNC-4 (Fig. S11b), the metal nanoparticles are dispersed in carbon skeleton and only a few hollow spheres are formed. When decreasing metal dosages, compared with CoFe-SNC-4, CoFe-SNC-3 shows the decreased metal nanoparticles and hollow structure (Fig. S11c). Further decreasing the metal dosage of CoFe-SNC results in the absence of metal nanoparticles and the formation of well-defined interconnected hollow spherical structure (Fig. S11d). Thus, the metal dosages exert an important influence on both the structural architecture and existence form of metal species, and further affects the ORR electrocatalytic activity. The CoFe-SNC with high onset potential (0.97 V) and $E_{1/2}$ (0.86 V) stands out as the best among the series and even suppresses the Pt/C (0.96 V and 0.82 V) as shown in Fig. 5a.

For comparison, SNC was prepared under the similar procedure to CoFe-SNC with the absence of Co and Fe sources. The SNC displays an onset potential of 0.92 V and $E_{1/2}$ of 0.63 V, while the $E_{1/2}$ of CoFe-NC is measured to be 0.82 V (Fig. 5a). In comparison to unsatisfied ORR activity of CoFe-NC and SNC, the positive $E_{1/2}$ and onset potential of CoFe-SNC suggest its high ORR activity. Furthermore, the kinetic currents (J_K) at different potentials are shown in Fig. 5b. It is clear that the ORR efficiency decreases in the order of CoFe-SNC, CoFe-NC and SNC. Upon S-doping, the J_K of CoFe-SNC is larger than the sum of CoFe-NC and SNC, signifying that the C-S-C and TM-N-C sites deliver a synergistic promotion on the intrinsic ORR activity. This upgraded electrocatalytic ability in terms of low overpotential to drive ORR on CoFe-SNC stands out as

the best among the reported TM-N-C catalysts (Table S1). The ORR process through a four-electron transfer pathway is highly desired. However, the side reaction with H_2O_2 product also occurs via two-electron transfer pathway. As indicated in Fig. 5c, the H_2O_2 yield for CoFe-SNC is lower than 10% with the electron transfer number (n) ranging from 3.87 to 3.93, signifying the predominant four-electron transfer pathway for ORR process. While the electron transfer number on the CoFe-NC ranges from 3.81 to 3.85 with an increased H_2O_2 yield relative to CoFe-SNC. The improved four-electron reaction pathway of CoFe-SNC can be attributed to the boosted intrinsic activity. In order to confirm the crucial role of S doping on boosting ORR activity of CoFe-SNC, a control sample CoFe-ONC was prepared in the similar procedure to that of CoFe-S-VXC except that the H_2O_2 -treated PS template was used to replace the H_2SO_4 -treated VXC. The high resolution XPS O 1 s spectra of CoFe-ONC is investigated and the O content is measured to be 5.9% (Fig. S12a). Similar to CoFe-SNC and CoFe-NC, the oxygen functionalities on CoFe-ONC consists of ketonic C=O (531.2 ± 0.3 eV) groups and epoxide C-O-C or hydroxyl C-OH (533.1 ± 0.3 eV) groups. In contrast to CoFe-NC, increased O contents on CoFe-ONC and CoFe-SNC indicate that both the H_2O_2 and H_2SO_4 treatment can incorporate oxygen functionalities on the catalysts surface and the fraction of C=O group on CoFe-ONC and CoFe-SNC are observed to consistently grow upon H_2O_2 and H_2SO_4 treatment. However, CoFe-ONC demonstrates an inferior activity to both of CoFe-NC and CoFe-SNC, accompanied with increased H_2O_2 yield (25%–12%) and reduced n (3.4–3.7) from 0 to 0.8 V (Fig. S12b and c). It is revealed that the introduction of oxygen functionalities leads to downgraded four-electron transfer ORR process. Thus, compared to CoFe-NC, the increased ORR activity of CoFe-SNC

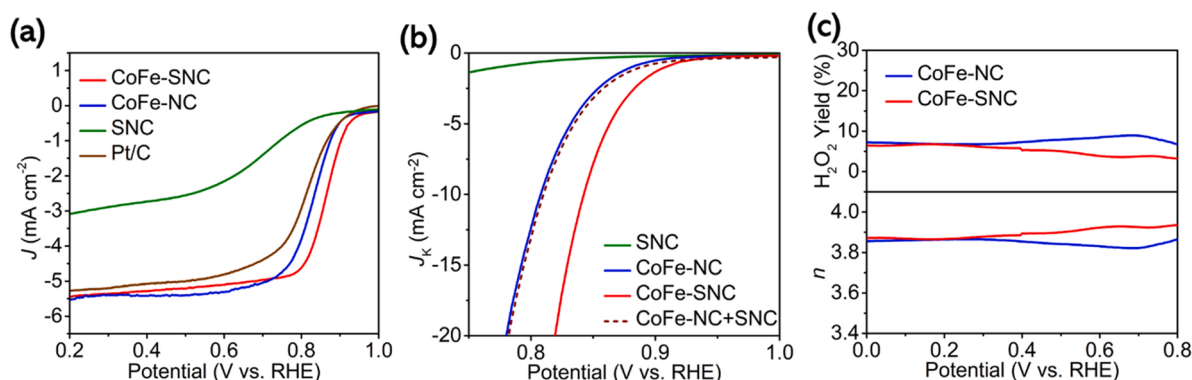


Fig. 5. Electrochemical measurement in O_2 -saturated 0.1 M KOH. (a) RDE polarization curves of CoFe-SNC, CoFe-NC, SNC and Pt/C at a scan rate of 10 mV s^{-1} and rotation speed of 1600 rpm, (b) kinetic current density of SNC, CoFe-NC, CoFe-SNC and CoFe-NC+ SNC, (c) H_2O_2 yield and transfer electron number of CoFe-NC and CoFe-SNC.

results from the S doping, instead of oxygen-functionalities. The formed C-S-C and TM-N-C sites can energetically drive ORR process synergistically.

The durability of CoFe-SNC for ORR was evaluated by chronoamperometric test. After experiencing a consecutive operation for 10 h, the ORR voltammetric current retains up to more than 87% with respect to the initial value (Fig. S13a). The TEM image after electrochemical durability test reveals that the hollow spherical structure can be well preserved after performance testing, indicating the superior structural robustness (Fig. S13b). The XPS data indicate that the changes of N species are not obvious. However, in the S 2p spectrum, a strong peak at 169.1 eV corresponds to oxidized sulfur, indicating that some of the C-S-C motif were oxidized (Fig. S13c, d). In contrast, the Pt/C delivers a retention of current approximately 77%, apparently manifesting the impressive durability of CoFe-SNC and remarkable potential in practical application.

Control experiments demonstrate that the SNC is failed to high-efficiently drive ORR process and CoFe-NC without S doping delivers a downgraded activity, highlighting that the coexistence of TM-N-C sites and C-S-C motif is of crucial importance for driving ORR process. The XPS measurement together with kinetic current analysis of SNC, CoFe-NC, CoFe-SNC and CoFe-NC+SNC indicate that C-S-C and TM sites with the long-range interaction gives rise to a synergistic promotion on the intrinsic ORR activity. The hollow structural architecture affords the adequate exposure of well-dispersed TM species as well as C-S-C motif as reflected by the HRTEM measurement. These results reveal the crucial role of well-dispersed TM-N-C species with S doping as active centers towards ORR. To confirm the important role of TM centers, KSCN poisoning experiments of CoFe-SNC was carried out. After treatment with potassium thiocyanate, CoFe-SNC retained well-defined hollow spherical structure but suffered from attenuated discharging performance (Fig. S14), which undoubtedly identified that the TM active sites with S-doping were responsible for the ORR activity for CoFe-SNC.

3.3. Mechanistic insight into the electrocatalytic properties of CoFe-SNC

To explore how the reaction interface and intrinsic catalytic ability influence the catalytic performances, another counterpart was synthesized under the similar procedure to CoFe-SNC except that the PS-200 was replaced by carbon block (VXC). The obtained CoFe-S-VXC features the solid granular morphology (Fig. S15a). The XRD pattern of CoFe-S-VXC reveals two diffraction peaks at 24.4° and 43.3° (2θ), corresponding to (002) and (101) planes of carbon, respectively (Fig. S15b). No diffraction peaks corresponding to metal-containing crystalline phases emerges, indicating the highly dispersed Co and Fe species in CoFe-S-VXC.

As shown in Fig. 6a, the CoFe-S-VXC delivers an unsatisfied ORR activity with respect to $E_{1/2}$ of 0.8 V and limited current density of 5 mA cm^{-2} . In comparison with the efficient-less ORR activity of CoFe-S-VXC, the CoFe-SNC exhibits rapid and steep ORR current increase, eventually delivering a high limited current density of 5.5 mA cm^{-2} . This superior ORR catalytic behavior is not possible to arise from an outstanding texture structure as the CoFe-SNC possesses a similar surface area and pore volume ($880 \text{ cm}^2/\text{g}$, $0.59 \text{ cm}^3/\text{g}$) to those of CoFe-S-VXC ($860 \text{ cm}^2/\text{g}$, $0.58 \text{ cm}^3/\text{g}$) (Fig. S16). Compared with CoFe-S-VXC, the hollow spherical architecture of CoFe-SNC with favorable curved surface enables a decent solid-liquid-gas triple-phase interface, which allows for the ample supply of gaseous reactant and unimpeded mass transfer during ORR process. Besides, upon S doping, CoFe-SNC demonstrates an $E_{1/2}$ of 0.86 V, exceeding CoFe-NC with an $E_{1/2}$ of 0.82 V. The synergistic promotion effect of S dopant and TM sites contributes to an upgraded ORR intrinsic activity of CoFe-SNC.

Furthermore, the Tafel analysis was implemented. The Tafel slopes are indicative of reactive resistance in ORR [51,52]. It can be observed in Fig. 6b that all the Tafel plots of CoFe-SNC, CoFe-NC and CoFe-S-VXC display two stages including low potential region and high potential region. At the stage of high potential, the reaction kinetics dominantly controls the overall oxygen electroreduction process. The ORR rate relies on the surface reaction which is driven by the intrinsic active sites [53]. The Tafel slopes of CoFe-SNC in high potential region is 78.7 mV dec^{-1} , which is lower than that of CoFe-NC (87.6 mV dec^{-1}), indicating that the favorable reaction kinetics is gifted by synergistic effect of C-S-C sites and TM-N-C active sites. At the stage of low potential, the ORR rate is mainly determined by the oxygen diffusion. The Tafel slopes of CoFe-SNC and CoFe-NC are calculated to be 630 and 684 mV dec^{-1} , both of which are obviously lower than that of CoFe-S-VXC (1459 mV dec^{-1}), suggesting that the mass transmission is promoted on both CoFe-SNC and CoFe-NC. The O_2 temperature-programmed desorption (O_2 -TPD) was performed to reveal the O_2 adsorption of as-prepared catalysts. In Fig. 7a, the pronounced peaks at 200°C is clearly observed on CoFe-NC and CoFe-SNC, which are associated with O_2 physisorption. This remarkable O_2 desorption signal is caused by the favorable hollow spherical architecture for O_2 trap and physisorption. It should be noted that in the range from 295 to 400°C , CoFe-SNC delivers the reinforced signal compared with CoFe-NC, verifying the increase in O_2 chemisorption on CoFe-SNC. The S doping into carbon skeleton on CoFe-SNC may afford a modulated electronic structure, which contributes to strengthening O_2 chemisorption. The enhanced O_2 chemisorption on CoFe-SNC exerts an important effect on constructing C-O interface during ORR process. The electrons can be transferred from carbon in CoFe-SNC to the chemically adsorbed oxygen to yield water. Combined with the Tafel slope analysis, it is demonstrated that CoFe-SNC shows an

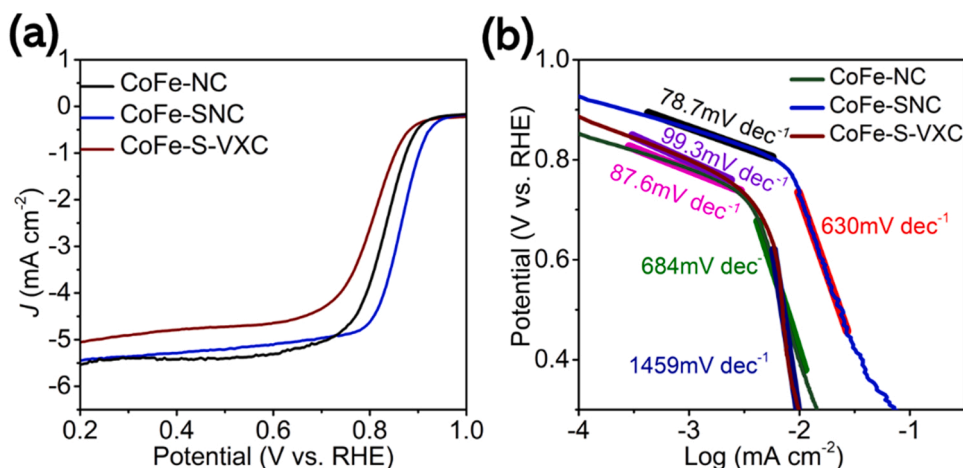


Fig. 6. (a) RDE polarization curves and (b) Tafel plots of CoFe-SNC, CoFe-NC and CoFe-S-VXC.

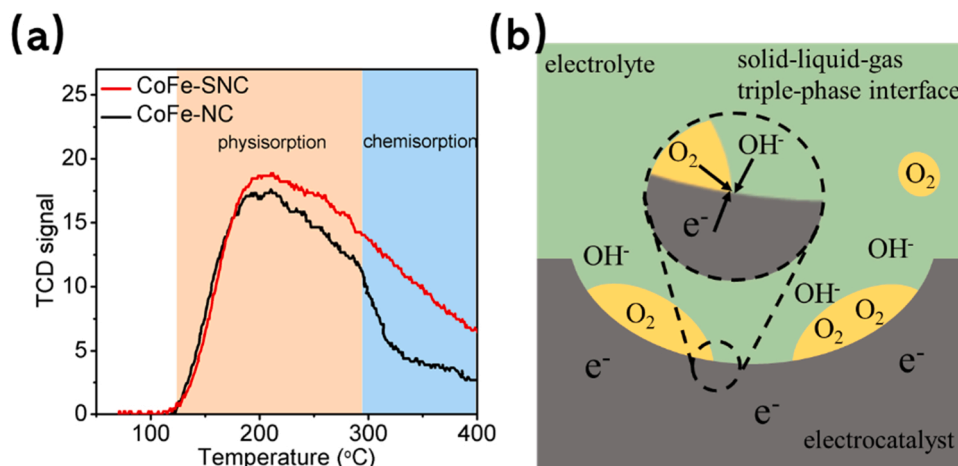


Fig. 7. (a) The O_2 -TPD curves for CoFe-NC and CoFe-SNC, (b) The schematic illumination of triple-phase electrocatalysis on CoFe-SNC.

accelerated reaction kinetics in terms of a low Tafel slope of 78.7 mV dec^{-1} in kinetics-controlled region, which results from the reinforced O_2 chemisorption. Also, the low resistance of O_2 transmission is reflected by low Tafel slope of 630 mV dec^{-1} in diffusion-controlled region of ORR on CoFe-SNC, which is closely related with the rapid entry and exit of reactants and products on optimized triple-phase interface due to the favorable O_2 physisorption (Fig. 7b).

The OER activity of CoFe-SNC and CoFe-S-VXC were also tested via conventional electrochemical test configuration in 0.1 M KOH electrolyte. CoFe-SNC delivers a current density of 10 mA cm^{-2} at the potential of 1.72 V (Fig. S17), which is lower than that of CoFe-S-VXC (1.83 V). CoFe-SNC and CoFe-S-VXC deliver different values of Tafel slopes during the OER process, suggesting the different OER kinetics. Compared to CoFe-S-VXC, the CoFe-SNC possesses a fast OER kinetics in terms of a low Tafel slope. Interestingly, when tested on a carbon paper, CoFe-SNC releases visible bubbles from the surface when the potential rises to 1.8 V (Fig. S18), followed by a steady increased current signal. Analog to the zeolite, it is considered that the as-formed O_2 molecule preferentially transfer to the available gas phase, rather than accumulate to yield bubble, thus giving rise to the apparent bubble at the beginning of OER process. This phenomenon is caused by the fact that hollow spherical structure with the gas-liquid-solid interface is capable of providing plentiful gas seed. The low overpotential for CoFe-SNC arises from the waived energy-consuming bubble formation process [37]. Furthermore, the durability of CoFe-SNC for OER was also evaluated. When manipulated in a chronoamperometric process at a fixed potential for OER, the current of CoFe-SNC after 10 h maintains the 93.3% of the initial value, while the IrO_2 displays the decreased current with 58.8% retention (Fig. S19). This signifies the good durability of CoFe-SNC for OER during longtime work.

To gain more insights into the outstanding electrocatalytic performance of CoFe-SNC, the electrochemical active surface area (ECSA) of the prepared samples were assessed via scan-rate-dependent cyclic voltammetry at non-Faradaic region (Fig. S20). As for an electrocatalyst, the ECSA represents the effective electrocatalytic active specific area during electrocatalytic reaction, which always inherently impact the electrocatalytic activity [54,55]. Obviously, the CoFe-SNC and CoFe-NC share the similar ECSA of 61.45 and 62.25 cm^2 respectively, both of which are larger than that of CoFe-S-VXC (31 cm^2). In this context, for both CoFe-SNC and CoFe-NC, the favorable gas-liquid-solid triple-phase interface enables a large available electrocatalytic active area and sufficient access of active sites. Compared with CoFe-NC, the enhanced electrocatalytic activity of CoFe-SNC can result from the boosted intrinsic reactivity of active sites. Thereby, the high electroactivity of CoFe-SNC is closely related with the boosted intrinsic activity and optimized reaction interface. The EIS was also measured for the

CoFe-SNC, CoFe-NC and CoFe-S-VXC (Fig. S21). The CoFe-S-VXC exhibits a low charge transport impedance as reflected by the small semicircle diameter, which can be caused by the incorporation of high electrically conductive VXC. It is worth noting that compared with CoFe-S-VXC, both CoFe-SNC and CoFe-NC possess the slightly increased charge transfer impedance with a little larger semicircle diameter than that of CoFe-S-VXC. This signifies that the CoFe-SNC derived from polydopamine possesses a considerable impedance during electron transport and the incorporation of S dopant is able to retain this favorable electron transmission.

The excellent performance of CoFe-SNC is rationalized to the ample gas-liquid-solid interface and decent intrinsic reactivity of active sites. The incorporation of S dopant not only makes a contribution on the promoting electrocatalytic activity of TM active sites but also affords a large surface area to host and highly-disperse active sites. The moderate surface curvature in hollow structure affords the Wenzel-Cassie coexistent state in which the solid surface is simultaneously covered by liquid and gas. The formation of ample triple-phase contact region allows for the sufficient supply of ORR/OER-relevant reactant and rapid exit of products. The advantageous reaction interface and favorable active sites jointly afford the CoFe-SNC with excellent electrochemical performance.

3.4. Zn-air battery performance

The bifunctional performance with respect of E_{gap} is presented in Table S1, and CoFe-SNC behaves comparably to or even surpasses those of state-of-art catalysts reported previously. A rechargeable liquid Zn-air battery was constructed to assess the practicability of ORR/OER bifunctionally active CoFe-SNC. The air cathode was fabricated by loading CoFe-SNC on the carbon paper and a Zn foil acted as anode with the electrolyte containing 6 M KOH and $0.2 \text{ M Zn}(\text{Ac})_2$ solution. The open circuit voltage of the Zn-air battery assembled with CoFe-SNC cathode is observed to be 1.45 V (Fig. 8a), while Pt/C gradually approaches 1.45 V after 30 min operation. Pt/C exhibits a peak power density of 66.9 mW cm^{-2} , while CoFe-SNC affords a high power density of 76.5 mW cm^{-2} with a corresponding current density of 163.9 mA cm^{-2} (Fig. 8b). Moreover, when discharging at 10 and 20 mA cm^{-2} , CoFe-SNC exhibits steady discharge voltages of 1.22 and 1.18 V , respectively, while Pt/C shows the discharge voltages of 1.19 and 1.10 V . After discharging at 10 mA cm^{-2} over 40.8 h , CoFe-SNC gives rise to a specific capacity of $636.3 \text{ mA h g}_{\text{Zn}}^{-1}$ with corresponding gravimetric energy density of $776.3 \text{ W h kg}_{\text{Zn}}^{-1}$ (Fig. 8c), which surpass those of Pt/C ($587.06 \text{ mA h g}_{\text{Zn}}^{-1}$, $698.6 \text{ W h kg}_{\text{Zn}}^{-1}$). The Zn-air battery performance of CoFe-SNC is comparable, even superior to those of previously reported metal-based air electrode catalysts

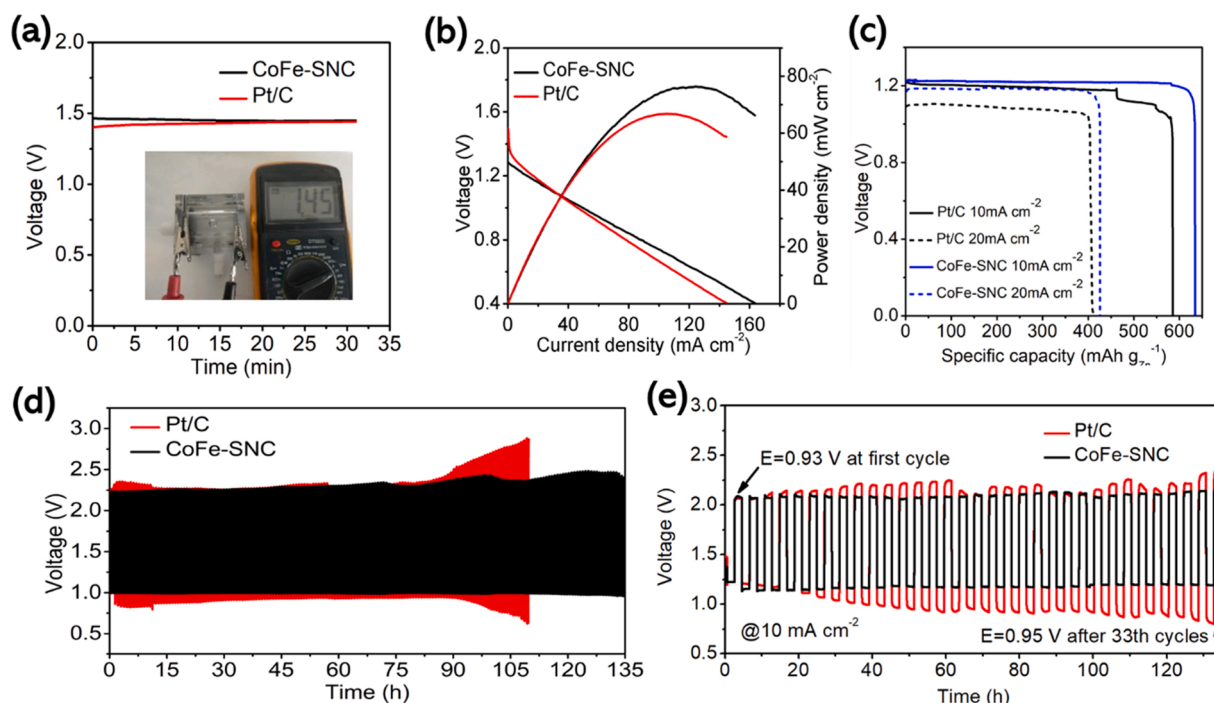


Fig. 8. (a) Open circuit plot of the as-assembled Zn-air battery with CoFe-SNC and Pt/C (inset: a photograph of Zn-air battery with CoFe-SNC). (b) Discharging polarization curves and corresponding power density curves of CoFe-SNC and Pt/C. (c) Specific capacity curves of CoFe-SNC and Pt/C at 10 and 20 mA cm⁻². (d) Long-term Charge-discharge cycling curves of rechargeable Zn-air batteries based on CoFe-SNC and Pt/C. (e) Charge-discharge cycling of Zn-air battery assembled by CoFe-SNC and Pt/C with 4 h for each cycle.

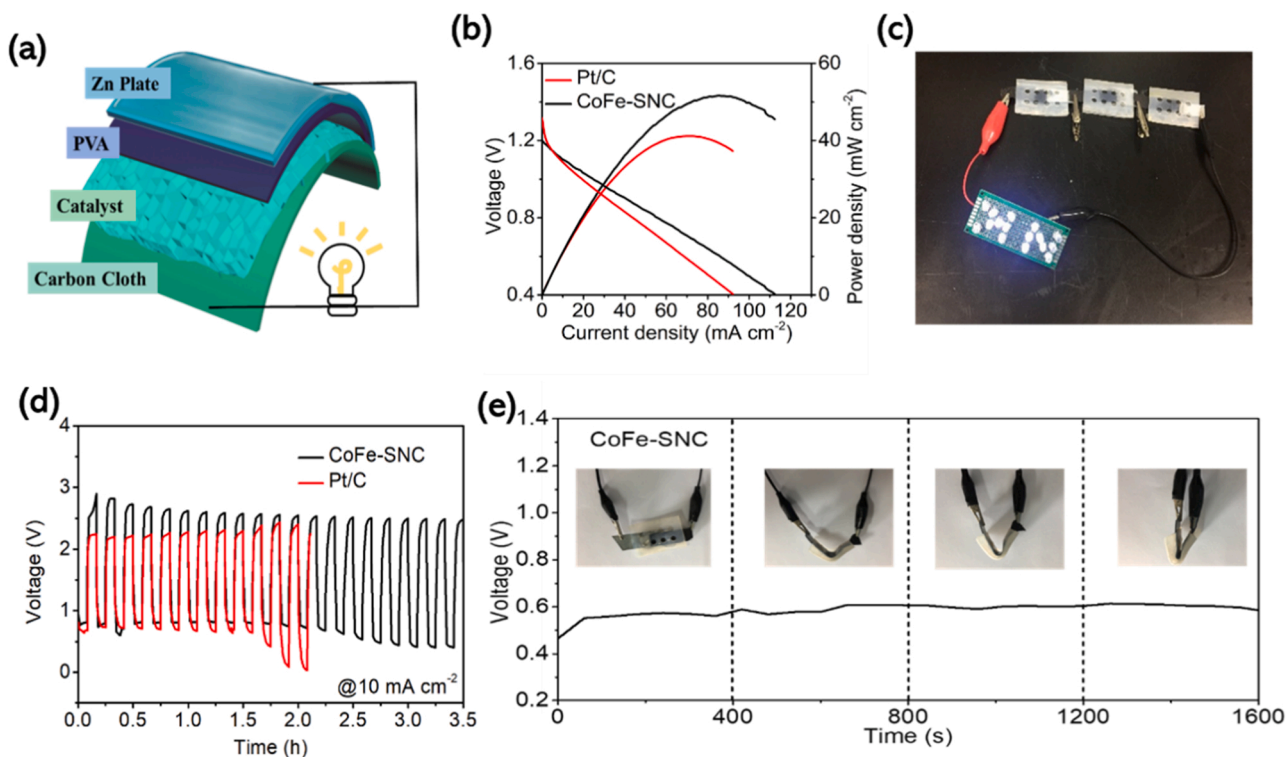


Fig. 9. (a) Scheme of the all-solid-state Zn-air batteries. (b) The polarization curves and corresponding power density plots of all-solid-state Zn-air batteries using CoFe-SNC and Pt/C as cathode catalysts. (c) A photograph of a LED illuminated by three all-solid-state Zn-air batteries in series. (d) Cycling performance of all-solid-state Zn-air batteries with a duration of 10 min per cycle at 10 mA cm⁻². (e) Photographs of the bending tests of the all-solid-state Zn-air batteries and corresponding galvanostatic discharge curves under various bending conditions at a current density of 10 mA cm⁻².

(Table S2). Besides, the rechargeability of CoFe-SNC air cathode was assessed by cycling test at 10 mA cm^{-2} with a cycle time of 40 min. Zn-air battery based on CoFe-SNC presents initial discharging voltage of 1.01 V and charging voltage of 2.20 V, affording a low voltage gap of 1.19 V. After continuous operation for 135 h, in contrast to regular decay of Pt/C (initial discharge-charge gap: 1.48 V; discharge-charge gap after continuous operation for 109 h: 2.24 V), CoFe-SNC delivers a neglectable decreased voltage gap of 1.14 V after 202 cycles, suggesting the outstanding stability of CoFe-SNC in Zn-air battery operation (Fig. 8d). Furthermore, the rechargeability of battery was evaluated for galvanostatically discharging and subsequently charging at 10 mA cm^{-2} for 4 h each step. CoFe-SNC exhibits a slight change of voltage gap from 0.93 to 0.95 V after 33 cycles, suggesting an impressive rechargeability, which is superior to that of Pt/C with respect to the gradual depression on the discharging-charging performance (Fig. 8e). These results reveal the great potential of CoFe-SNC to act as efficient cathodic materials as the alternative of precious metal-based catalysts for sustainable energy conversion and storage technique. Multiple Zn-air batteries in series can provide specific power in practical implementation. One proof-of-concept illustration is to light a commercial red light emitting diode (LED). In Fig. S22, two Zn-air batteries with CoFe-SNC air electrode in series could continuously light the LED (working voltage: nearly 2.8 V), manifesting its promising implementation for Zn-air batteries.

The PS templates with sizes of 50, 500 and 4000 nm were subjected to the sulfuric acid leaching and were employed as hard templates to prepare CoFe-SNC-50, CoFe-SNC-500 and CoFe-SNC-4000. As reflected in Fig. S23, the CoFe-SNC demonstrates the lowest charge-discharge voltage gap (1.31 V) at the current density of 50 mA cm^{-2} among the series, indicating that the electrochemical performance contribution of moderate surface curvature in hollow spherical architecture is well maintained after the incorporation of S dopant.

In order to demonstrate the potential of CoFe-SNC for flexible and portable electronic devices, the all-solid-state Zn-air battery consisting of CoFe-SNC air cathode, alkaline polyvinyl alcohol (PVA) electrolyte and zinc anode was constructed (Fig. 9a). The all-solid-state Zn-air battery assembled by CoFe-SNC with a high open-circuit voltage of 1.34 V (Fig. S24) delivers a peak power density of 51.5 mW cm^{-2} , which is higher than that of Pt/C (40 mW cm^{-2}) (Fig. 9b). As shown in Fig. 9c, when employed for actual application, three all-solid-state Zn-air batteries with CoFe-SNC in series can power a LED. The long-term cycling performance of battery equipped with CoFe-SNC was assessed by the galvanostatic discharge-charge cycling at a 10 mA cm^{-2} with a cycling rate of 10 min per cycle. Slight change in the charging-discharging voltage gap is observed on CoFe-SNC after 3.5 h continuous operation, while Pt/C shows the attenuated performance after 2 h continuous operation. Although the superior cycling performance of CoFe-SNC to that of Pt/C, it should be noted that there is much room to improve the long-term cycling performance (Fig. 9d). By taking advantage of the flexible all-solid-state configuration, the battery with CoFe-SNC air electrode is able to discharge at 10 mA cm^{-2} stably at different bending states, implying the remarkable potential in electronics and wearable-electronics implementation (Fig. 9e).

4. Conclusions

The functionalized bimetallic electrocatalyst (CoFe-SNC) with S-dopant modification and well-constructed hollow sphere structure was developed. By rationally regulating the surface curvature of hollow spherical electrocatalyst, it is demonstrated that the underwater microenvironment in terms of gas (O_2), liquid (electrolyte), solid (electrocatalyst) triple-phase interface can exert significant effect on the cathodic process of Zn-air batteries due to the fact that actual discharging/charging reactions occur at the solid-liquid-gas triple-phase contact region. Meanwhile, the intrinsic electrocatalytic activity modulated by the synergistic effect between C-S-C and TM sites via long-range interaction flourishes the electrochemical activity. Thus, resulting

from the boosted intrinsic catalytic activity, smooth mass transmission and high access of active sites, the excellent electrochemical activity and Zn-air battery performance are realized. It is expected that this functionalized electrocatalyst holds great promise to be the alternate for precious metal catalysts in energy-related fields.

CRediT authorship contribution statement

Chen-Chen Weng: Conceptualization, Methodology, Investigation, Writing – original draft. **Jin-Tao Ren:** Investigation, Formal analysis. **Hao-Yu Wang:** Investigation. **Xian-Wei Lv:** Investigation. **Yue-Jun Song:** Investigation. **Yan-Su Wang:** Investigation. **Lei Chen:** Investigation. **Wen-Wen Tian:** Investigation. **Zhong-Yong Yuan:** Supervision, Writing – review & editing.

Declaration of Competing Interest

The authors declare that they have no known competing financial interests or personal relationships that could have appeared to influence the work reported in this paper.

Acknowledgements

This work was supported by the National Natural Science Foundation of China (22179065, 22111530112, 21875118) and the Natural Science Foundation of Tianjin (19JCZDJC37700).

Appendix A. Supporting information

Supplementary data associated with this article can be found in the online version at doi:10.1016/j.apcatb.2022.121190.

References

- [1] T. Zhou, N. Zhang, C. Wu, Y. Xie, Surface/interface nanoengineering for rechargeable Zn-air batteries, *Energy Environ. Sci.* 13 (2020) 1132–1153, <https://doi.org/10.1039/c9ee03634b>.
- [2] X.X. Wang, M.T. Swihart, G. Wu, Achievements, challenges and perspectives on cathode catalysts in proton exchange membrane fuel cells for transportation, *Nat. Catal.* 2 (2019) 578–589, <https://doi.org/10.1038/s41929-019-0304-9>.
- [3] P. Prabhu, V. Jose, J.M. Lee, Design strategies for development of TMD-based heterostructures in electrochemical energy systems, *Matter* 2 (2020) 526–553, <https://doi.org/10.1016/j.matt.2020.01.001>.
- [4] V. Jose, J.M.V. Nsanizimana, H. Hu, J. Choi, X. Wang, J.M. Lee, Highly efficient oxygen reduction reaction activity of N-doped carbon-cobalt boride heterointerfaces, *Adv. Energy Mater.* 11 (2021), 2100157, <https://doi.org/10.1002/aenm.202100157>.
- [5] H. Wang, J. Li, K. Li, Y. Lin, J. Chen, L. Gao, V. Nicolosi, X. Xiao, J.M. Lee, Transition metal nitrides for electrochemical energy applications, *Chem. Soc. Rev.* 50 (2021) 1354–1390, <https://doi.org/10.1039/D0CS00415D>.
- [6] X. Hu, Y. Chen, M. Zhang, G. Fu, D. Sun, J.M. Lee, Y. Tang, Alveolate porous carbon aerogels supported Co9S8 derived from a novel hybrid hydrogel for bifunctional oxygen electrocatalysis, *Carbon* 144 (2019) 557–566, <https://doi.org/10.1016/j.carbon.2018.12.099>.
- [7] G. Fu, J. Wang, Y. Chen, Y. Liu, Y. Tang, J.B. Goodenough, J.M. Lee, Exploring indium-based ternary thiospinel as conceivable high-potential air-cathode for rechargeable Zn-air batteries, *Adv. Energy Mater.* 8 (2018), 1802263, <https://doi.org/10.1002/aenm.201802263>.
- [8] G. Fu, X. Yan, Y. Chen, L. Xu, D. Sun, J.M. Lee, Y. Tang, Boosting bifunctional oxygen electrocatalysis with 3D graphene aerogel-supported Ni/MnO particles, *Adv. Mater.* 30 (2018), 1704609, <https://doi.org/10.1002/adma.201704609>.
- [9] P. Prabhu, J.M. Lee, Metalloenes as functional materials in electrocatalysis, *Chem. Soc. Rev.* 50 (2021) 6700–6719, <https://doi.org/10.1039/D0CS01041C>.
- [10] C. Chen, Y. Kang, Z. Huo, Z. Zhu, W. Huang, H.L. Xin, J.D. Snyder, D. Li, J. A. Herron, M. Mavrikakis, M. Chi, K.L. More, Y. Li, N.M. Markovic, G.A. Somorjai, P. Yang, V.R. Stamenkovic, Highly crystalline multimetallic nanoframes with three-dimensional electrocatalytic surfaces, *Science* 343 (2014) 1339–1343, <https://doi.org/10.1126/science.1249061>.
- [11] J.T. Ren, G.G. Yuan, C.C. Weng, Z.Y. Yuan, Rationally designed Co3O4-C nanowire arrays on Ni foam derived from metal organic framework as reversible oxygen evolution electrodes with enhanced performance for Zn-air batteries, *ACS Sustain. Chem. Eng.* 6 (2018) 707–718, <https://doi.org/10.1021/acssuschemeng.7b03034>.
- [12] W. Wang, Q. Jia, S. Mukerjee, S. Chen, Recent insights into the oxygen-reduction electrocatalysis of Fe/N/C materials, *ACS Catal.* 9 (2019) 10126–10141, <https://doi.org/10.1021/acscatal.9b02583>.

- [13] H. Wang, J. Chen, Y. Lin, X. Wang, J. Li, Y. Li, L. Gao, L. Zhang, D. Chao, X. Xiao, J. M. Lee, Electronic modulation of non-Van der Waals 2D electrocatalysts for efficient energy conversion, *Adv. Mater.* 33 (2021), e2008422, <https://doi.org/10.1002/adma.202008422>.
- [14] C. Tang, H.F. Wang, Q. Zhang, Multiscale principles to boost reactivity in gas-involving energy electrocatalysis, *Acc. Chem. Res.* 51 (2018) 881–889, <https://doi.org/10.1021/acs.accounts.7b00616>.
- [15] J. Sun, N. Guo, T. Song, Y.R. Hao, J. Sun, H. Xue, Q. Wang, Revealing the interfacial electron modulation effect of CoFe alloys with CoCX encapsulated in N-doped CNTs for superior oxygen reduction, *Adv. Powder Mater.* (2021), <https://doi.org/10.1016/j.apmate.2021.11.009>.
- [16] W. Xu, Z. Lu, X. Sun, L. Jiang, X. Duan, Superwetting electrodes for gas-involving electrocatalysis, *Acc. Chem. Res.* 51 (2018) 1590–1598, <https://doi.org/10.1021/acs.accounts.8b00070>.
- [17] J.E. George, S. Chidangil, S.D. George, Recent progress in fabricating superaerophobic and superaerophilic surfaces, *Adv. Mater. Interfaces* 4 (2017), 1601088, <https://doi.org/10.1002/admi.201601088>.
- [18] P. Wang, T. Hayashi, Q. Meng, Q. Wang, H. Liu, K. Hashimoto, L. Jiang, Highly boosted oxygen reduction reaction activity by tuning the underwater wetting state of the superhydrophobic electrode, *Small* 13 (2017), <https://doi.org/10.1002/smll.201601250>.
- [19] J. Liu, D. Zhu, Y. Zheng, A. Vasileff, S.Z. Qiao, Self-supported earth-abundant nanoarrays as efficient and robust electrocatalysts for energy-related reactions, *ACS Catal.* 8 (2018) 6707–6732, <https://doi.org/10.1021/acscatal.8b01715>.
- [20] J. Chen, C. Fan, X. Hu, C. Wang, Z. Huang, G. Fu, J.M. Lee, Y. Tang, Hierarchically porous Co/Cox My(M = P, N) as an efficient Mott-Schottky electrocatalyst for oxygen evolution in rechargeable Zn-air batteries, *Small* 15 (2019), e1901518, <https://doi.org/10.1002/smll.201901518>.
- [21] J.D. Yi, R. Xu, Q. Wu, T. Zhang, K.T. Zang, J. Luo, Y.L. Liang, Y.B. Huang, R. Cao, Atomically dispersed iron–nitrogen active sites within porphyrinic triazine-based frameworks for oxygen reduction reaction in both alkaline and acidic media, *ACS Energy Lett.* 3 (2018) 883–889, <https://doi.org/10.1021/acsenenergylett.8b00245>.
- [22] Y. Ye, H. Li, F. Cai, C. Yan, R. Si, S. Miao, Y. Li, G. Wang, X. Bao, Two-dimensional mesoporous carbon doped with Fe–N active sites for efficient oxygen reduction, *ACS Catal.* 7 (2017) 7638–7646, <https://doi.org/10.1021/acscatal.7b02101>.
- [23] J.T. Ren, Z.Y. Yuan, A universal route to N-coordinated metal anchored on porous carbon nanosheets for highly efficient oxygen electrochemistry, *J. Mater. Chem. A* 7 (2019) 13591–13601, <https://doi.org/10.1039/c9ta03300a>.
- [24] Z. Li, X. Wu, X. Jiang, B. Shen, Z. Teng, D. Sun, G. Fu, Y. Tang, Surface carbon layer controllable Ni3Fe particles confined in hierarchical N-doped carbon framework boosting oxygen evolution reaction, *Adv. Powder Mater.* (2021), <https://doi.org/10.1016/j.apmate.2021.11.007>.
- [25] V. Jose, H. Hu, E. Edison, W. Manalastas Jr., H. Ren, P. Kidkhunthod, S. Sreejith, A. Jayakumar, J.M.V. Nsanzimana, M. Srinivasan, J. Choi, J.M. Lee, Modulation of single atomic Co and Fe sites on hollow carbon nanospheres as oxygen electrodes for rechargeable Zn-air batteries, *Small Methods* 5 (2021), e2000751, <https://doi.org/10.1002/smt.202000751>.
- [26] L. Wei, H.E. Karahan, S. Zhai, H. Liu, X. Chen, Z. Zhou, Y. Lei, Z. Liu, Y. Chen, Amorphous bimetallic oxide-graphene hybrids as bifunctional oxygen electrocatalysts for rechargeable Zn-air batteries, *Adv. Mater.* 29 (2017), <https://doi.org/10.1002/adma.201701410>.
- [27] S. Li, C. Cheng, X. Zhao, J. Schmidt, A. Thomas, Active salt/silica-templated 2D mesoporous FeCo-Nx-Carbon as Bifunctional Oxygen Electrodes for Zinc-air Batteries, *Angew. Chem. Int. Ed.* 57 (2018) 1856–1862, <https://doi.org/10.1002/anie.201710852>.
- [28] Q. Zhou, S. Hou, Y. Cheng, R. Sun, W. Shen, R. Tian, J. Yang, H. Pang, L. Xu, K. Huang, Y. Tang, Interfacial engineering Co and MnO within N,S co-doped carbon hierarchical branched superstructures toward high-efficiency electrocatalytic oxygen reduction for robust Zn-air batteries, *Appl. Catal. B Environ.* 295 (2021), 120281, <https://doi.org/10.1016/j.apcatb.2021.120281>.
- [29] G. Fu, Y. Wang, Y. Tang, K. Zhou, J.B. Goodenough, J.M. Lee, Superior oxygen electrocatalysis on nickel indium thiospinels for rechargeable Zn-air batteries, *ACS Mater. Lett.* 1 (2019) 123–131, <https://doi.org/10.1021/acsmaterialslett.9b00093>.
- [30] X.W. Lv, Y. Liu, Y.S. Wang, X.L. Liu, Z.Y. Yuan, Encapsulating vanadium nitride nanodots into N,S-codoped graphitized carbon for synergistic electrocatalytic nitrogen reduction and aqueous Zn-N2 battery, *Appl. Catal. B Environ.* 280 (2021), 119434, <https://doi.org/10.1016/j.apcatb.2020.119434>.
- [31] Q. Wei, G. Zhang, X. Yang, Y. Fu, G. Yang, N. Chen, W. Chen, S. Sun, Litchi-like porous Fe/N/C spheres with atomically dispersed FeNx promoted by sulfur as highly efficient oxygen electrocatalysts for Zn-air batteries, *J. Mater. Chem. A* 6 (2018) 4605–4610, <https://doi.org/10.1039/c7ta08746b>.
- [32] H.J. Shen, E. Gracia-Espino, J.Y. Ma, K.T. Zang, J. Luo, L. Wang, S.S. Gao, X. Mamat, G.Z. Hu, T. Wagberg, S.J. Guo, Synergistic effect between the atomically dispersed active site of Fe–N–C and C–S–C for ORR in acidic medium, *Angew. Chem. Int. Ed.* 56 (2017) 13800–13804, <https://doi.org/10.1002/anie.201706602>.
- [33] Y. Han, Y. Wang, R. Xu, W. Chen, L. Zheng, A. Han, Y. Zhu, J. Zhang, H. Zhang, J. Luo, C. Chen, Q. Peng, D. Wang, Y. Li, Electronic structure engineering to boost oxygen reduction activity by controlling the coordination of the central metal, *Energy Environ. Sci.* 11 (2018) 2348–2352, <https://doi.org/10.1039/c8ee01481g>.
- [34] D.H. Kwak, S.B. Han, Y.W. Lee, H.S. Park, I.A. Choi, K.B. Ma, M.C. Kim, S.J. Kim, D. H. Kim, J.I. Sohn, K.W. Park, Fe/N/S-doped mesoporous carbon nanostructures as electrocatalysts for oxygen reduction reaction in acid medium, *Appl. Catal. B Environ.* 203 (2017) 889–898, <https://doi.org/10.1016/j.apcatb.2016.10.084>.
- [35] D. Quéré, J.M. Di Meglio, F. Brochard-Wyart, Spreading of liquids on highly curved surfaces, *Science* 249 (1990) 1256–1260, <https://doi.org/10.1126/science.249.4974.1256>.
- [36] J.T. Ren, C.Y. Wan, T.Y. Pei, X.W. Lv, Z.Y. Yuan, Promotion of electrocatalytic nitrogen reduction reaction on N-doped porous carbon with secondary heteroatoms, *Appl. Catal. B Environ.* 266 (2020), 118633, <https://doi.org/10.1016/j.apcatb.2020.118633>.
- [37] J.L. Wilbur, H.A. Biebuyck, J.C. MacDonald, G.M. Whitesides, Scanning force microscopies can image patterned self-assembled monolayers, *Langmuir* 11 (1995) 825–831, <https://doi.org/10.1021/la00003a025>.
- [38] Y. Zhang, Y. Chu, Y. Yang, L. Dong, F. Yang, J. Liu, Fabrication of polystyrene–PbS core-shell and hollow PbS microspheres with sulfonated polystyrene templates, *Colloid Polym. Sci.* 285 (2007) 1061–1066, <https://doi.org/10.1007/s00396-007-1664-2>.
- [39] S. Chen, J. Li, Y. Zhu, Z. Guo, S. Su, Increasing the efficiency of intumescent flame retardant polypropylene catalyzed by polyoxometalate based ionic liquid, *J. Mater. Chem. A* 1 (2013) 15242–15246, <https://doi.org/10.1039/c3ta13538a>.
- [40] L. Hadidi, E. Davari, M. Iqbal, T.K. Purkait, D.G. Ivey, J.G. Veinot, Spherical nitrogen-doped hollow mesoporous carbon as an efficient bifunctional electrocatalyst for Zn-air batteries, *Nanoscale* 7 (2015) 20547–20556, <https://doi.org/10.1039/c5nr06028a>.
- [41] X. Yu, H. Fan, Y. Liu, Z. Shi, Z. Jin, Characterization of carbonized polydopamine nanoparticles suggests ordered supramolecular structure of polydopamine, *Langmuir* 30 (2014) 5497–5505, <https://doi.org/10.1021/la500225v>.
- [42] M.G. Park, D.U. Lee, M.H. Seo, Z.P. Cano, Z. Chen, 3D ordered mesoporous bifunctional oxygen catalyst for electrically rechargeable zinc-air batteries, *Small* 12 (2016) 2707–2714, <https://doi.org/10.1002/smll.201600051>.
- [43] F. Hu, H. Yang, C. Wang, Y. Zhang, H. Lu, Q. Wang, Co–N-doped mesoporous carbon hollow spheres as highly efficient electrocatalysts for oxygen reduction reaction, *Small* 13 (2017), 1602507, <https://doi.org/10.1002/smll.201602507>.
- [44] W. Wang, W. Chen, P. Miao, J. Luo, Z. Wei, S. Chen, NaCl crystallites as dual-functional and water-removable templates to synthesize a three-dimensional graphene-like macroporous Fe–N–C catalyst, *ACS Catal.* 7 (2017) 6144–6149, <https://doi.org/10.1021/acscatal.7b01695>.
- [45] S. Li, C. Cheng, X.J. Zhao, J. Schmidt, A. Thomas, Active salt/silica-templated 2D mesoporous FeCo-Nx-carbon as bifunctional oxygen electrodes for zinc-air batteries, *Angew. Chem. Int. Ed.* 57 (2018) 1856–1862, <https://doi.org/10.1002/anie.201710852>.
- [46] M.C. Biesinger, B.P. Payne, A.P. Grosvenor, L.W.M. Lau, A.R. Gerson, R.S.C. Smart, Resolving surface chemical states in XPS analysis of first row transition metals, oxides and hydroxides: Cr, Mn, Fe, Co and Ni, *Appl. Surf. Sci.* 257 (2011) 2717–2730.
- [47] U. I. S. R. N.H. W. L. K. Surface states and reactivity of pyrite and marcasite, *Appl. Surf. Sci.* 179 (2001) 222–229, <https://doi.org/10.1016/j.apsusc.2010.10.051>.
- [48] J.T. Ren, L. Chen, D.D. Yang, Z.Y. Yuan, Molybdenum-based nanoparticles (Mo2C, MoP and MoS2) coupled heteroatoms-doped carbon nanosheets for efficient hydrogen evolution reaction, *Appl. Catal. B Environ.* 263 (2020), 118352, <https://doi.org/10.1016/j.apcatb.2019.118352>.
- [49] B.Q. Li, C.X. Zhao, J.N. Liu, Q. Zhang, Electrosynthesis of hydrogen peroxide synergistically catalyzed by atomic Co–Nx–C sites and oxygen functional groups in noble-metal-free electrocatalysts, *Adv. Mater.* 31 (2019), e1808173, <https://doi.org/10.1002/adma.201808173>.
- [50] Y.P. Zhu, T.Y. Ma, T.Z. Ren, J. Li, G.H. Du, Z.Y. Yuan, Highly dispersed photoactive zinc oxide nanoparticles on mesoporous phosphonated titania hybrid, 156 (2014) 44–52, DOI: [10.1016/j.apcatb.2014.03.001](https://doi.org/10.1016/j.apcatb.2014.03.001).
- [51] J. Liang, Y. Zheng, J. Chen, J. Liu, D. Hulicova-Jurcakova, M. Jaroniec, S.Z. Qiao, Facile oxygen reduction on a three-dimensionally ordered macroporous graphitic C3N4/carbon composite electrocatalyst, *Angew. Chem. Int. Ed.* 51 (2012) 3892–3896, <https://doi.org/10.1002/anie.201107981>.
- [52] Y.J. Song, J.T. Ren, G. Yuan, Y. Yao, X. Liu, Z.Y. Yuan, Facile synthesis of Mo2C nanoparticles on N-doped carbon nanotubes with enhanced electrocatalytic activity for hydrogen evolution and oxygen reduction reactions, *J. Energy Chem.* 38 (2019) 68–77, <https://doi.org/10.1016/j.jechem.2019.01.002>.
- [53] B.X.R. Wu, Q. Gao, Y.R. Zheng, X.S. Zheng, J.F. Zhu, M.R. Gao, S.H. Yu, A janus nickel cobalt phosphide catalyst for high-efficiency neutral-pH water splitting, *Angew. Chem. Int. Ed.* 130 (2018) 15671–15675, <https://doi.org/10.1002/anie.201808929>.
- [54] J.T. Ren, Z.Y. Yuan, Direct synthesis of nitrogen, phosphorus and sulfur tri-doped carbon nanorods as highly efficient oxygen reduction and evolution electrocatalysts, *ChemCatChem* 10 (2018) 3260–3268, <https://doi.org/10.1002/cctc.201702000>.
- [55] Q. Hu, G. Li, G. Li, X. Liu, B. Zhu, X. Chai, Q. Zhang, J. Liu, C. He, Trifunctional electrocatalysis on dual-doped graphene nanorings-integrated boxes for efficient water splitting and Zn-air batteries, *Adv. Energy Mater.* 9 (2019), 1803867, <https://doi.org/10.1002/aenm.201803867>.